Incoherent Thomson scattering diagnostics in non-relativistic current-carrying plasmas

IPP report

Omar Maj[1,2] and Roberto Bilato[1]

[1] *Max-Planck-Institut für Plasmaphysik, Garching.*
[2] *Max-Planck-Institut für Sonnensystemforschung, Katlenburg-Lindau.*
e-mail: omaj@ipp.mpg.de, rbb@ipp.mpg.de

1. Outline. In this note, we specialize the theory of Thompson scattering measurements of electron distribution functions to the case of the experimental setup proposed by Kantor [1] for the ASDEX Upgrade tokamak; these calculations have been used in the feasibility study by Tsalas et al. [2]. More specifically, we begin from the theory reported by Sheffield [3] for the scattered power, and we follow closely the analysis of Segre [4, 5]; then, we compute the signal to noise ratio (SNR) as in the work of Carretta *et al.* [6].

In our analysis, we assume that electrons are well described by the Spitzer and Härm distribution function [7]; such an assumption is common in the Thomson scattering literature [5, 6], though it implies that trapping effects, due to the inhomogeneous magnetic field of a tokamak, as well as relativistic effects, are neglected. Moreover, strictly speaking, the use of the Spitzer-Härm electron distribution function is justified for an Ohmic current density only, i.e., a current density driven by an external electric field. A more precise analysis would require a detailed modeling of the electron distribution function, which could be obtained, e.g., by solving the Fokker-Planck equation in the drift approximation.

In order to understand how far the results depend on the considered model of electron distribution function, we study a class of distributions obtained as perturbations of the Maxwellian distribution. Despite being limited to small electron drift velocities (as compared to the electron thermal speed), such a perturbation argument allows us to carry out explicit analytical calculations. Both the Spitzer-Härm and the shifted Maxwellian distributions can be approximated in this way in the limit of small drift velocity.

2. A bird-eye-view of Thomson scattering. To shorten a long story, let us begin from equation (27) of Sheffield [3], which gives the electromagnetic power $P_s(\omega_s, \vec{v})d\Omega$ scattered within the solid-angle element $d\Omega$ at the frequency ω_s by an electron located at a given spatial point, with initial velocity $\vec{v}$, and accelerated by an incident monochromatic electromagnetic wave beam of frequency

ω_i, namely,

$$P_s(\omega_s, \vec{v})d\Omega = \frac{P_i}{A}\, r_0^2\, \frac{\omega_s^3}{\omega_i^3}\, \left(1 + \frac{v}{c}\right) d\Omega. \tag{1}$$

Here, and throughout this note, the subscripts i and s refer to quantities of the incident and scattered radiation, respectively. In equation (1), c denotes the speed of light, and $P_i = (c/8\pi)E_i^2 A$ is the total electric-field power carried by the incident beam with electric field amplitude E_i and cross-section area A, while r_0^2 is the Thomson cross section, with $r_0 = 2.82 \cdot 10^{-13}$cm being the classical electron radius. This result retains relativistic effects up to first-order terms in $\beta = v/c$.

The difference in frequency between the incident and the scattered radiation is due to Doppler shift, cf. equation (9) of Sheffield [3],

$$\omega_s = \omega_i \frac{1 - \hat{\imath} \cdot \vec{v}/c}{1 - \hat{s} \cdot \vec{v}/c}, \tag{2}$$

where $\hat{\imath} = \vec{k}_i/k_i$ and $\hat{s} = \vec{k}_s/k_s$ stand for the unit vectors of the incident and scattering (observation) direction, respectively, while $\vec{v}$ is the velocity of the electron. Here, the electromagnetic radiation is described by plane waves in free space (this is possible in view of the high frequency of the beam). Thus, the incident and scattered wave vectors, $\vec{k}_i$ and $\vec{k}_s$, have length $k_i = \omega_i/c$ and $k_s = \omega_s/c$, respectively, while equation (2) can be rewritten in the form

$$\omega_s - \omega_i = \left(\vec{k}_s - \vec{k}_i\right) \cdot \vec{v} = \vec{k} \cdot \vec{v}, \tag{3}$$

which means that, given a fixed incident frequency ω_i, the scattered radiation at the frequency ω_s comes from the electrons with a precise velocity component along the direction of the differential wave vector $\vec{k} = \vec{k}_s - \vec{k}_i$, namely,

$$v_k = \hat{k} \cdot \vec{v} = \Delta\omega/k, \qquad \Delta\omega = \omega_s - \omega_i. \tag{4}$$

According to equation (3) a single electron produces a spectral power distribution (power per unit frequency interval) given by

$$\left[P_s(\omega_s, \vec{v})d\Omega\right]\delta(\omega_s - \omega_i - kv_k) = \left[P_s(\omega_s, \vec{v})d\Omega\right]k^{-1}\delta(v_k - \Delta\omega/k),$$

where we have used the transformation properties of the Dirac delta function. (It is worth recalling that delta functions are dimensional objects and carry the dimensions of the inverse of their argument).

The total *incoherent* contribution to the electromagnetic power *per unit frequency interval* of the electrons contained in a small scattering volume V, centered around the probed point, amounts to

$$\bar{P}_s(\omega_s)d\Omega = V n_{\rm e} \int \left[P_s(\omega_s, \vec{v})d\Omega\right]k^{-1}\delta(v_k - \Delta\omega/k) f(\vec{v}) d^3v, \tag{5}$$

where $n_{\rm e}$ is the electron number density and $f(\vec{v})$ is the electron distribution function, satisfying the normalization condition $\int f(\vec{v})d^3v = 1$, both being considered approximately independent of the position in the scattering volume.

Since we are interested in the periphery of the plasma column where the electron temperature attains modest values, we can consider, as an order-of-magnitude analysis, the totally non-relativistic limit $\beta = v/c \ll 1$ in the whole

range of electron velocity probed by the Thomson scattering diagnostics; hence, the correction terms of order β will be dropped in the subsequent analysis. For such non-relativistic electrons, equation (2) implies $\omega_s - \omega_i = O(\beta)$, hence, $\omega_s \approx \omega_i$, which, on the other hand, means $k_i \approx k_s$. As a consequence of this approximation, if θ is the angle between $\vec{k}_i$ and $\vec{k}_s$, the amplitude of the differential wave vector $\vec{k} = \vec{k}_s - \vec{k}_i$ is

$$k = 2k_i \sin\big(\theta/2\big). \tag{6}$$

In addition, in view of the non-relativistic approximation, equation (1) simplifies further,

$$P_s(\omega_s, \vec{v})d\Omega \approx \frac{P_i}{A} r_0^2 d\Omega. \tag{7}$$

Those approximations can be used into (5), with the result that the factor $\big[P_s(\omega_s, \vec{v})d\Omega\big]k^{-1}$ can be regarded as approximately independent of the electron velocity, thus, significantly simplifying the velocity integral.

More specifically, upon choosing a reference frame such that the unit vector $\hat{e}_z$ of the third axis is $\hat{e}_z = \hat{k}$, the remaining integral amounts to $h(\Delta\omega/k)$, where the function

$$h(v_k) = \int_{-\infty}^{+\infty} \int_{-\infty}^{+\infty} f(v_x, v_y, v_k) dv_x dv_y, \tag{8}$$

is the projection of the distribution function along the direction of $\hat{e}_z = \hat{k}$. With τ_L and $\Delta\Omega$ being the total time in which photons are collected and the solid angle of the line of sight, respectively, we can write the collected energy per unit frequency interval, namely,

$$\mathcal{E}_s(\omega_s) = \tau_L \bar{P}_s(\omega_s)\Delta\Omega = V n_\mathrm{e} \tau_L \big[\frac{P_i}{A} r_0^2 \Delta\Omega\big] k^{-1} h(\Delta\omega/k). \tag{9}$$

After dividing the total energy per unit frequency interval by the energy of a single detected photon $\hbar\omega_s$, we obtain the number of photons that enter the detector, namely,

$$\frac{\mathcal{E}_s(\omega_s)}{\hbar\omega_s} = n_\mathrm{e} \Big[\frac{\tau_L P_i}{\hbar\omega_s}\Big] r_0^2 L \Delta\Omega k^{-1} h(\Delta\omega/k),$$

where $L = V/A$ is the length of the scattering region. On using again the approximation $\omega_s \approx \omega_i$, the factor between square brackets amounts to

$$\frac{\tau_L P_i}{\hbar\omega_s} \approx \frac{\mathcal{E}_i}{\hbar\omega_i},$$

which is the total number of incident photons, $\mathcal{E}_i$ being the total output energy of the laser during the time τ_L.

The photons actually converted into photoelectrons and, thus, detected are, however, less than those that enter the detector due to the quantum efficiency of the detector (η) as well as to the efficiencies of both the transmission (ρ) and the receiving (χ) optical lines [6]. Correcting for the efficiencies, the number of scattering photoelectrons per unit frequency interval collected by the detector as a function of the scattered angular frequency is

$$N_{\mathrm{sc},\omega}(\omega_s) = (\eta\rho\chi) n_\mathrm{e} \frac{\mathcal{E}_i}{\hbar\omega_i} r_0^2 L \Delta\Omega k^{-1} h(\Delta\omega/k). \tag{10}$$

One can see that the observed signal is proportional to the projection $h(v_k)$ of the electron distribution function evaluated at $v_k = \Delta\omega/k$. Let us note, however, that, when relativistic corrections are accounted for, the simple proportionality relationship (10) is lost, as approximations (6) and (7) can no longer be exploited, the scattering signal being then expressed in terms of a convolution integral of the power spectrum with the electron distribution function, cf. equation (5).

3. Number and electric current density measurements. With an *absolute* calibration of the detectors, it is possible to determine the electron density n_e from the zeroth-order moment of $N_{\mathrm{sc},\omega}(\omega_s)$, namely,

$$n_\mathrm{e} = \frac{1}{H}\int N_{\mathrm{sc},\omega}(\omega_s)d\omega_s, \tag{11}$$

where the constant

$$H = (\eta\rho\chi)\frac{\mathcal{E}_i}{\hbar\omega_i}r_0^2 L\Delta\Omega, \tag{12}$$

is known from the specifications of the laser and the characteristics of the diagnostics setup.

The z-component of the electron current density, that is, the component along the direction of the differential wave vector $\vec{k} = \vec{k}_s - \vec{k}_i$, can be estimated from the first-order moment of $N_{\mathrm{sc},\omega}(\omega_s)$ [5, 8],

$$j_z = \frac{e}{H}\int \frac{\omega_s - \omega_i}{k} N_{\mathrm{sc},\omega}(\omega_s)d\omega_s, \tag{13}$$

e being the elementary charge. When only a *relative* calibration of the detectors is available, it is still possible to determine j_z, if n_e can be measured with another diagnostics.

4. The electron distribution function of Spitzer and Härm. In order to determine when the signal-to-noise ratio (SNR) is sufficiently high to make the measurement of the electric current density possible, we start the analysis from the expected theoretical distribution function in presence of an electric field $\vec{E}$. When $|\vec{E}|$ is smaller than the Dreicer field $E_D = m_\mathrm{e}v_\mathrm{th}\nu_\mathrm{coll}/e$, a reasonable approximation [5] of $f(\vec{v})$ is the Spitzer-Härm electron distribution function [7]

$$f_\mathrm{SH}(\vec{v}) = \frac{1}{\pi^{3/2}v_\mathrm{th}^3}e^{-v^2/v_\mathrm{th}^2}\Big[1 + D(v/v_\mathrm{th})\cos\alpha_v\Big]; \tag{14}$$

here, m_e is the electron mass, $v_\mathrm{th} = \sqrt{2k_B T_\mathrm{e}/m_\mathrm{e}}$ is the electron thermal speed, ν_coll the electron collisional frequency, $v^2 = v_x^2 + v_y^2 + v_z^2$, $v_z = v_k$, and α_v is the velocity pitch-angle, i.e., the angle between $\vec{E}$ and $\vec{v}$. Figure 1 represents the geometry of a generic setup.

The deformation function $D(x)$ in equation (14) depends on the effective charge $Z = \sum_j n_j Z_j^2/n_\mathrm{e}$, where the index j labels ion species with charge $Z_j e$ and density n_j. Upon following the approach of Segre [5], we write

$$D(x) = (v_D/v_\mathrm{th})qg(x),$$

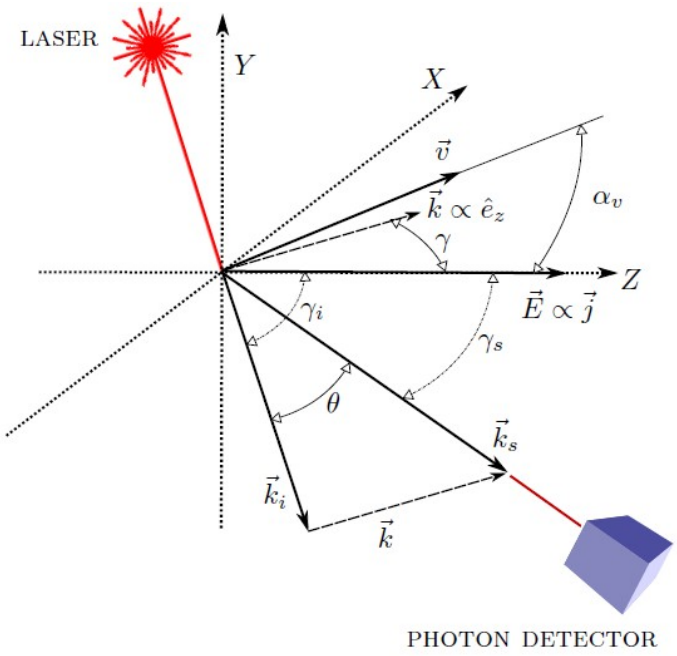

Figure 1: Scattering geometry represented in the laboratory coordinates (X, Y, Z), with Z oriented along the direction of the current density. The two angles γ_i and γ_s, between the current density $\vec{j}$ and the two wave vectors $\vec{k}_i$ and $\vec{k}_s$, respectively, together with the angle θ, between $\vec{k}_i$ and $\vec{k}_s$, are determined by the direction of the incident laser beam and by the line of sight of the detector.

where $\vec{v}_D = \vec{j}/(en_e)$ is the electron drift velocity associated to the current density $\vec{j}$ driven by the electric field. The function $g(x)$ is tabulated in reference [7] for $Z = 1, 2, 4, 16, \infty$, and the coefficient q takes the values [5]

$$q = 0.7619,\ 0.6485,\ 0.5645,\ 0.4803,\ 0.4431,$$

respectively, in correspondence of the considered values of Z.

Alladio and Martone [9] have derived the plasma current values from the Thomson scattering signals assuming both a shifted Maxwellian and Spitzer-Härm distribution functions: the values obtained with the latter assumption are in a much better agreement with the measurements done with coil probes.

In the calculation of $h(v_k)$ in equation (8), it is convenient to orient the axes so that the unit vector $\hat{e}_x$ is perpendicular to the plane defined by $\vec{k}$ and $\vec{E}$, while $\hat{e}_z = \hat{k}$, as before, and $\hat{e}_y = \hat{e}_z \times \hat{e}_x$, cf. figure 2; then, the function $h(v_k)$ takes the form

$$h_{\mathrm{SH}}(v_k) = \frac{1}{\sqrt{\pi} v_{\mathrm{th}}} e^{-v_k^2/v_{\mathrm{th}}^2} + \frac{(v_D/v_{\mathrm{th}})q}{\pi^{3/2} v_{\mathrm{th}}^3} \int_{-\infty}^{+\infty} dv_x \int_{-\infty}^{+\infty} dv_y e^{-v^2/v_{\mathrm{th}}^2} g\Big(\frac{v}{v_{\mathrm{th}}}\Big) \cos\alpha_v.$$

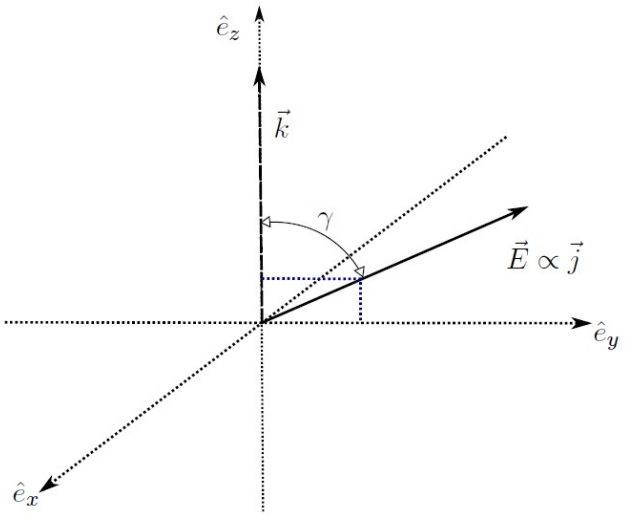

Figure 2: The reference frame $\{\hat{e}_x, \hat{e}_y, \hat{e}_z\}$. The z-axis is parallel to the differential wave vector $\vec{k} = \vec{k}_s - \vec{k}_i$, with the current density lying in the z-y plane. The physical orientations of the vectors $\vec{k}$ and $\vec{j}$ are shown in figure 1 above.

With γ being the angle between $\vec{E}$ and $\vec{k}$, one has $\vec{E}/E = (0, \sin\gamma, \cos\gamma)$,

$$\cos\alpha_v = \frac{\vec{E}\cdot\vec{v}}{Ev} = \frac{v_y}{v}\sin\gamma + \frac{v_k}{v}\cos\gamma,$$

and the integral then splits into the sum of two terms proportional to $\sin\gamma$ and $\cos\gamma$; the integrand of the former, however, is odd and the corresponding integral vanishes with the result that

$$\begin{aligned} h_{\rm SH}(v_k) &= \frac{1}{v_{\rm th}}\tilde{h}_{\rm SH}\Big(\frac{v_k}{v_{\rm th}}\Big) \\ &= \frac{1}{\sqrt{\pi}v_{\rm th}} e^{-v_k^2/v_{\rm th}^2}\left[1 + \frac{v_D}{v_{\rm th}}\cos\gamma\,\mathcal{P}\Big(\frac{v_k}{v_{\rm th}}\Big)\right], \end{aligned} \tag{15}$$

where we have introduced the function (slightly different from the corresponding quantity in the work of Segre [5])

$$\mathcal{P}(x) = 2qxe^{x^2}\int_{|x|}^{\infty} e^{-w^2} g(w)dw. \tag{16}$$

Figure 3 shows the function $\mathcal{P}(x)/(2x)$ for $Z = 1, 2, 4, 16, \infty$, with $g(x)$ calculated by interpolation of the values given in Table 1 of reference [7]. The function $\mathcal{P}(x)$ represents the part of the signal due to the presence of an electric current density, properly normalized to the driving $(v_D/v_{\rm th})\cos\gamma$; in order to highlight the behavior near $x = 0$, we plot $\mathcal{P}(x)/(2x)$, which is an even function ($\mathcal{P}$ is odd), hence the positive domain $x \geq 0$ only is shown. As expected, the deformation of the signal due to the current density increases with the frequency

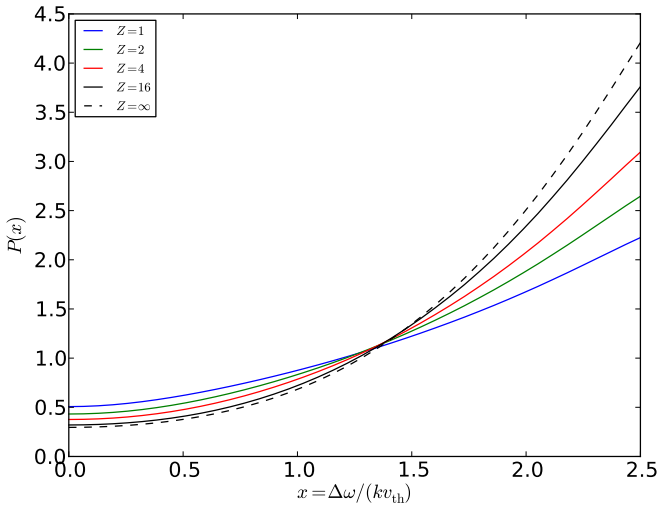

Figure 3: The function $P(x) = \mathcal{P}(x)/(2x)$, with $\mathcal{P}(x)$ defined in equation (16), using the values computed by Spitzer and Härm [7] for different values of the effective charge Z.

shift $x = \Delta\omega/(kv_{\rm th})$, i.e., it is large on the tail of the measured spectrum, where, on the other hand, the number of collected photoelectrons drops.

Therefore, the feasibility of the measure, i.e., the possibility of distinguishing a Spitzer-Härm distribution from a Maxwellian distribution, depends on the balance between the magnitude of the deformation and the statistics of the signal: where the statistics is good the deformation is small, and vice versa.

Let us compute the number of detected photoelectrons per unit frequency interval by assuming the Spitzer-Härm distribution for the probed electrons. According to equation (10), that is given by

$$N_{{\rm sc},\omega}(\omega_s) = (\eta\rho\chi) n_{\rm e} \frac{\mathcal{E}_i}{\hbar\omega_i} r_0^2 L \Delta\Omega \frac{1}{kv_{\rm th}} \tilde{h}_{\rm SH}\Big(\frac{\Delta\omega}{kv_{\rm th}}\Big), \tag{17}$$

where $\Delta\omega = \omega_s - \omega_i$ is the frequency shift of the scattered radiation. In the experimental practice, the probed frequency interval is divided into a number of discrete spectral channels so small that $N_{{\rm sc},\omega}$ can be considered constant within each channel. Hence, the number of photoelectrons detected in a spectral channel of width $\Delta\omega_s$ centered around the frequency ω_s is given by

$$N_{\rm sc}(\omega_s) = (\eta\rho\chi) n_{\rm e} \frac{\mathcal{E}_i}{\hbar\omega_i} r_0^2 L \Delta\Omega \frac{\Delta\omega_s}{kv_{\rm th}} \tilde{h}_{\rm SH}\Big(\frac{\Delta\omega}{kv_{\rm th}}\Big). \tag{18}$$

In order to compute this number, we need to evaluate the width $\Delta\omega_s$ of the channel. Typically, the spectral width is given in terms of the wave length, and one has

$$\Delta\omega_s \approx \frac{2\pi c}{\lambda_i^2}\Delta\lambda_s, \quad \text{or} \quad \frac{\Delta\omega_s}{\omega_i} \approx \frac{\Delta\lambda_s}{\lambda_i}. \tag{19}$$

The latter identity suggests that it is convenient to express the number of detected photoelectrons in each spectral channel as a function of $\Delta\omega/\omega_i$, and that

reads, upon making use of equation (6),

$$N_{\rm sc}(\omega_s) = (\eta\rho\chi) n_{\rm e} \frac{\mathcal{E}_i}{\hbar\omega_i} r_0^2 L \Delta\Omega \frac{c/v_{\rm th}}{2\sin(\theta/2)} \frac{\Delta\omega_s}{\omega_i} \tilde{h}_{\rm SH}\Big(\frac{c/v_{\rm th}}{2\sin(\theta/2)} \frac{\Delta\omega}{\omega_i}\Big), \qquad (20)$$

where $c/v_{\rm th} = (0.5 \cdot 511/T_{\rm e}[\text{keV}])^{1/2}$.

Particularly, let us note that the result of equation (20) can be rather sensitive to the scattering angle θ in view of the factor $1/\sin(\theta/2)$ both in front of and in the argument of the function $\tilde{h}_{\rm SH}$.

5. Signal-to-noise ratio and modeling of the background light. There are at least two sources of noise in the measurement of $N_{\rm sc}(\omega_s)$, [4]: the statistical fluctuations of the number of photoelectrons and the background radiation emitted by the plasma (mainly due to stray radiation and bremsstrahlung; an estimate of the latter is given in equation (3) of reference [10]). If $N_{\rm b}$ is the number of background photoelectrons collected by the detector, the signal-to-noise ratio of this measurement is [10],

$$\text{SNR} = \frac{N_{\rm sc}}{\sqrt{N_{\rm sc} + 2N_{\rm b}}}. \qquad (21)$$

The particular expression of the denominator (i.e., the noise) can be understood if one considers that, in practice, the signal $N_{\rm sc}$ is the result of two measurements: that of the total collected photoelectrons $N_{\rm sc} + N_{\rm b}$ and that of the background $N_{\rm b}$. We recall that the probability distribution of photoelectron counting is Poissonian (at least for an ideal counting), thus the statistical fluctuations of a number N of counts is given by the standard deviation $\sqrt{N}$ of the Poissson distribution; therefore, Poissonian standard deviations of these two measurements are $\sqrt{N_{\rm sc} + N_{\rm b}}$ and $\sqrt{N_{\rm b}}$, respectively. Assuming that the two measurements are statistically uncorrelated, the variance of the difference $N_{\rm sc} = (N_{\rm sc} + N_{\rm b}) - N_{\rm b}$ amounts to the sum of the variances, namely, $N_{\rm sc} + 2N_{\rm b}$, and the corresponding standard deviation gives the denominator in equation (21).

In a Thomson scattering experiment, the noise is typically dominated by the background term, hence, a realistic estimate of $N_{\rm b}$ is crucial for a quantitative analysis. We need to specify a model for the number $N_{{\rm b},\omega}$ of background photoelectrons per unit frequency interval, from which we have $N_{\rm b} = N_{{\rm b},\omega}\Delta\omega_s$, with $\Delta\omega_s$ being the width of each spectral channel. With the due exception of a narrow interval around the laser frequency ω_i, where the stray radiation is so high that an appropriate filter must be applied, thus, excluding that interval from the measurement, the background $N_{{\rm b},\omega}$ is usually found to be constant on the spectral band actually observed by the diagnostics. We choose to specify such a constant as a fraction of the average scattering signal over one thermal width [11], namely,

$$\overline{N}_{{\rm sc},\omega} = \frac{1}{2\Delta\omega_{\rm th}} \int N_{{\rm sc},\omega} d\omega_s,$$

where $\Delta\omega_{\rm th} = k v_{\rm th}$ is the band width corresponding to one thermal speed, cf. equation (10). Strictly speaking, the integration should be limited to the interval $|\omega_s - \omega_i| \leq \Delta\omega_{\rm th}$, but we extend that to the whole observed frequency

range for convenience; as a consequence, $N_{\mathrm{b},\omega} = \mu_{\mathrm{b}} \overline{N}_{\mathrm{sc},\omega}$ and

$$N_{\mathrm{b}} = \mu_{\mathrm{b}} \frac{\Delta\omega_s}{2\Delta\omega_{\mathrm{th}}} N_{\mathrm{sc,tot}},$$

where $N_{\mathrm{sc,tot}}$ is the total number of scattering photoelectrons collected by the diagnostics, and μ_{b} is a free parameter that characterizes the background level of the considered experimental setup.

It is worth noting that, since N_{b} has been considered constant, the total number of collected background photoelectrons is proportional to the width of the spectral band observed by the diagnostics; it is, therefore, not always convenient to increase the band-width. More specifically, if the observed frequency interval is $[\omega_i - \Delta\omega_{\mathrm{tot}}, \omega_i + \Delta\omega_{\mathrm{tot}}]$, the total number of collected photoelectrons is $N_{\mathrm{b,tot}} = \mu_{\mathrm{b}} N_{\mathrm{sc,tot}} \Delta\omega_{\mathrm{tot}} / \Delta\omega_{\mathrm{th}}$. It is convenient to define the half-width $\Delta\omega_{\mathrm{tot}}$ in terms of $\Delta\omega_{\mathrm{th}}$, namely, $\Delta\omega_{\mathrm{tot}} = \xi \Delta\omega_{\mathrm{th}}$, hence, $N_{\mathrm{b,tot}} = \mu_{\mathrm{b}} \xi N_{\mathrm{sc,tot}}$. The choice of the parameter ξ is crucial for a correct analysis of the data and will be discussed in the next two sections.

6. Results for the new setup in ASDEX Upgrade using the Spitzer-Härm distribution function. Let us specialize our analysis to the case of the proposed ASDEX Upgrade setup [2]. With reference to figure 1, the laboratory coordinates (X, Y, Z) are such that Z points along the toroidal direction, while X and Y span the poloidal plane; the laser beam impinges vertically from the top, hence $\gamma_i = 90°$, and the detector is placed so that $\theta = 90°$ and $\gamma_s = 18°$. Among the proposed scenarios, we consider those corresponding to the following parameters:

- electron density $n_{\mathrm{e}} = 2.5 \cdot 10^{13} \mathrm{cm}^{-3}$;
- electron temperature $T_{\mathrm{e}} = 500\mathrm{eV}$ and $700\mathrm{eV}$;
- drift velocity $v_D / v_{\mathrm{th}} = 0.02,\ 0.03,\ 0.05$;
- effective charge $Z = 1$;
- solid angle $\Delta\Omega = 0.01\mathrm{sr}$;
- scattering length $L = 2.0\mathrm{cm}$;
- incidence angle $\gamma_i = 90°$;
- line-of-sight angle $\gamma_s = 18°$;
- scattering angle $\theta = 90°$;
- laser energy $\mathcal{E}_i = 20\mathrm{J}$;
- laser wave length $\lambda_i = 694.3\mathrm{nm}$;
- width of spectral channels $\Delta\lambda_s = 2\mathrm{nm}$;
- spectral band of the diagnostics $\xi = v_{\mathrm{max}} / v_{\mathrm{th}} = 2.0$;
- efficiencies $\eta\rho\chi \approx 0.03$, [11];
- filter $-0.0134 \leq \Delta\omega/\omega_i \leq 0.0154$, [11];

- background photoelectrons $\mu_\mathrm{b} = 1/10$, [11].

From the three angles γ_i, γ_s, and θ, one can compute γ in equation (15): by definition, we have $\vec{j} \cdot \vec{k} = jk \cos\gamma$, and

$$\vec{j} \cdot \vec{k} = \vec{j} \cdot \vec{k}_s - \vec{j} \cdot \vec{k}_i \approx j k_i \big(\cos\gamma_s - \cos\gamma_i \big),$$

with the non-relativistic approximation $k_s \approx k_i$; equation (6) then gives,

$$\cos\gamma = \frac{\cos\gamma_s - \cos\gamma_i}{2\sin(\theta/2)}, \tag{22}$$

and, for the foregoing parameters, one finds $\gamma = 47.74°$.

The given laser energy refers to a single pulse. If the repetition rate of the laser is high enough, however, it is possible to collect photons from a whole burst of several laser pulses, thus, increasing the total laser output energy $\mathcal{E}_i$ at the price of a reduced temporal resolution.

The parameter ξ, which determines the band-width of the diagnostics, has been defined in section 5 together with the background level μ_b. Particularly, ξ controls how many thermal widths are included in the observed spectral band: the higher is ξ the lower is the discretization error [8], i.e., the error associated to replacing the integral (13) by a discrete sum over a finite number of channels; on the other, hand, increasing ξ will increase the number of collected background photoelectrons. Therefore, there is a trade off between the discretization error and the background light. An appropriate choice of this parameter in the analysis of the experimental data depends on the expected theoretical form of the electron distribution function: when the deformation of the electron distribution function, due to the presence of an electron drift velocity, occurs mainly in the bulk, it will suffice to take into account a few spectral channels; on the other hand, when the deformation occurs on the tails, more spectral channels are needed. In the specific case of the Spitzer-Härm distribution function, the deformation, i.e., the function $D(v/v_\mathrm{th})$ in equation (14), is vanishingly small in the bulk, hence, we have to pick the relatively high value of $\xi = 2$, which, for the considered setup, corresponds to 87 and 103 spectral channels for $T_\mathrm{e} = 500$eV and 700eV, respectively. (Anyway, the value of ξ must be such that the argument x of the function $\mathcal{P}(x)$ stays well within the range tabulated by Spitzer and Härm [7]; this gives the upper limit $\xi \leq 3.2$.)

In figure 4, the Thomson scattering signal (20) is shown as a function of the normalized frequency shift $\Delta\omega/\omega_i$ (red curves) for $T_\mathrm{e} = 500$eV and for different values of $v_D/v_\mathrm{th} = 0.02$, 0.03, and 0.05, together with the signal produced by the corresponding Maxwellian distribution (blue dots), and the background level (magenta dashed curve); we recall that the value of v_D/v_th in the experimental setup considered by Tsalas et al. [2] falls within the interval $[0.005, 0.06]$; the reference scenario corresponds to the value 0.02, while the high value of 0.05 is shown here just as an example. Analogously, figure 5 shows the same quantities for the higher electron temperature $T_\mathrm{e} = 700$eV. The most important information in figures 4 and 5 is the signal-to-noise ratio (SNR). We recall that a threshold of SNR≥ 2 is usually required for reliable measurements [6], and this requirement is satisfied in the considered cases.

From a physical point of view, let us note that the higher is v_D/v_th the more the signal differs from the corresponding Maxwellian distribution, though

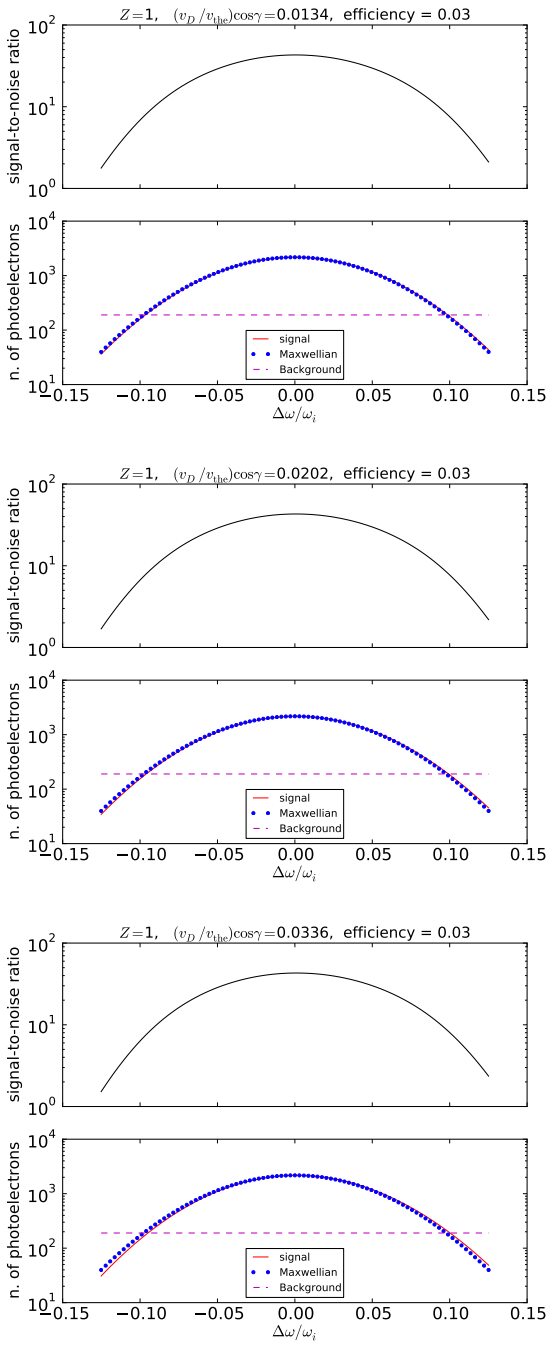

Figure 4: Thomson scattering signals (red curves) according to equation (20) with $T_{\rm e} = 500$eV and $v_D/v_{\rm th} = 0.02$ (upper panel), $v_D/v_{\rm th} = 0.03$ (central panel), and $v_D/v_{\rm th} = 0.05$ (lower panel). Here, $Z = 1$. Each signal is compared to the corresponding Maxwellian (blue dots), to the constant background light (magenta dashed line), and to the signal-to-noise ratio (21).

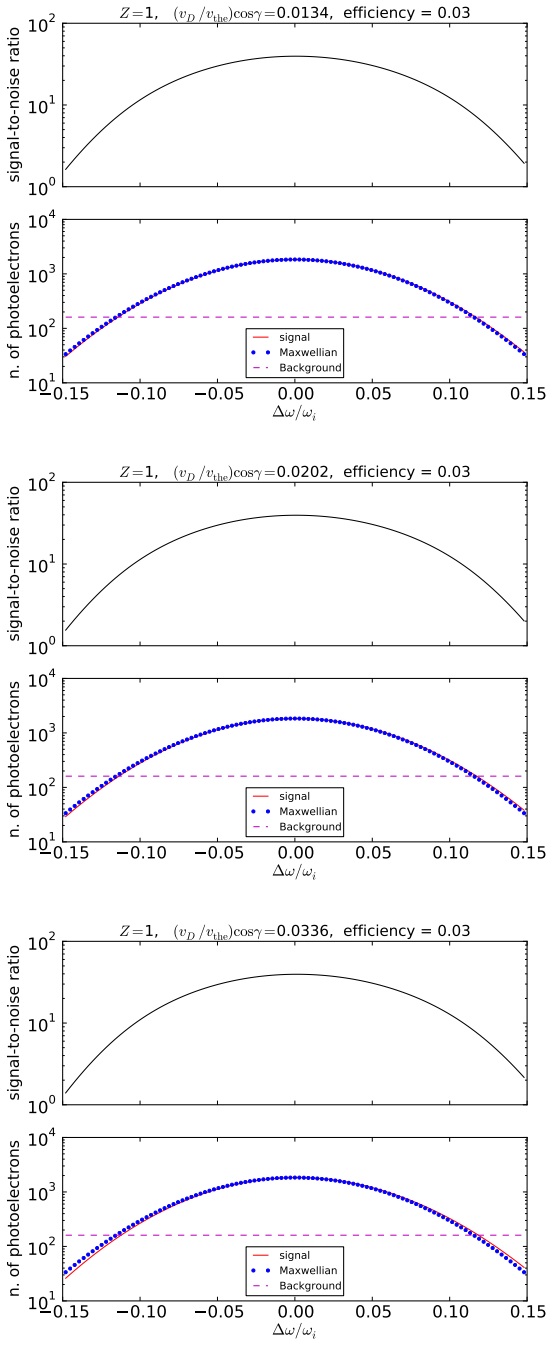

Figure 5: The same as in figure 4, but with $T_{\rm e} = 700$eV.

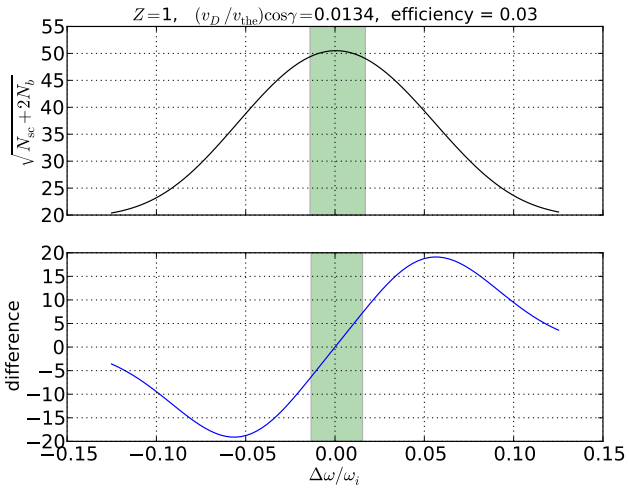

Figure 6: Difference between the Spitzer-Härm signal and the corresponding Maxwellian signal according to equation (20) (lower panel) together with the statistical error $\sqrt{N_{\rm sc}+2N_{\rm b}}$ (upper panel) for $T_{\rm e}=500$eV, and $v_D/v_{\rm th}=0.02$. The green shadowed area denotes the part of the spectrum which is cut off by the filter of the diagnostics. It is worth noting that one thermal speed corresponds to $\Delta\omega/\omega_i\approx 0.06$, and that is the approximate location of the maximum of the signal difference.

the differences are tiny. On comparing figure 4 with figure 5, we note that the dependence on the temperature is weak: the number of collected photoelectrons slightly decreases with the temperature in agreement with the factor $c/v_{\rm th}$ in equation (20). One can verify that the dependence on the effective charge Z is weak as well, except on the very tails of the distribution function; this can be understood by inspection of the function $\mathcal{P}(x)$ defined in equation (16) and represented in figure 3 for different values of Z.

In order to be quantitative, the difference between the Spitzer-Härm signal and the corresponding Maxwellian signal is displayed in figure 6 together with the statistical error $\sqrt{N_{\rm sc}+2N_{\rm b}}$ for the reference case $T_{\rm e}=500$eV, $v_D/v_{\rm th}=0.02$; the estimate of the total number of collected scattering photoelectrons (integrated over all spectral channels) in this case amounts to $8.242\cdot 10^4$, which is one order of magnitude lower then the number foreseen by Kantor [1]; such a discrepancy in the total number of collected photoelectrons is due to the value of the laser energy [2], which was one order of magnitude larger in previous estimates [1] (accounting for a burst of several pulses). The total number of background photoelectrons is found to be $1.651\cdot 10^4$, in agreement with the relation given at the end of section 5. The green shadowed area shows the part of the signal which is cut off by the filter of the diagnostics: that corresponds to the maximum of the distribution function where the deformation due to the presence of a current density is small. Let us remark that this depends strongly on the scattering angle θ: for small values of θ the width of the distribution decreases significantly, cf. the argument of $\tilde{h}_{\rm HS}$ in equation (20). Figure 6 clearly shows that, for the considered value $v_D/v_{\rm th}=0.02$, the fluctuations are

larger than the signal difference.

In order to understand the consequences of the results of figure 6, given the signal (20) produced by a Spitzer-Härm distribution function, it is possible to simulate the measure of the plasma electric current density. Indeed, we can compute j_z by approximating equation (13) with the sum over spectral channels, namely, [8]

$$j_z \approx \frac{ec}{H2\sin(\theta/2)} \sum_{\text{channels}} \frac{\Delta\omega}{\omega_i} N_{\text{sc}}(\omega_s). \tag{23}$$

For the case of figure 6, for which, in particular, $v_D/v_{\text{th}} = 0.02$, the result of the discrete sum (23) is in agreement with the relationship $v_D \cos(\gamma) = j_z/(en_{\text{e}})$, which comes from the definition of v_D, within an error of $\sim 9.3\%$. Such an error can be regarded as an estimate of the discretization error [8] coming from the substitution of the integral (13) with the discrete sum (23) over a finite number of spectral channels (for the considered channel width $\Delta\lambda_s = 2\text{nm}$ and bandwidth $\xi = 2$ of the simulated diagnostics). One can verify that the discretization error depends in a non-trivial way on the temperature as well as on the geometry of the experimental setup.

In this simulated measure, the noise can be estimated by computing the error due to the expected fluctuations of the number of photoelectrons, namely, $\sqrt{N_{\text{sc}} + 2N_{\text{b}}}$. The absolute error associated to each of the term of the sum (23) is

$$\frac{ec}{H2\sin(\theta/2)} \frac{|\Delta\omega|}{\omega_i} \sqrt{N_{\text{sc}} + 2N_{\text{b}}}.$$

More precisely, this is the standard deviation of the statistical distribution of the contribution of each channel to the current density. The standard deviation of the current density is then obtained as the square root of the sum of variances of each channel, assuming that channels are statistically uncorrelated. The relative error on the electric current density then reads

$$\Delta j_z/j_z = \frac{\sqrt{\sum |\Delta\omega|^2 (N_{\text{sc}} + 2N_{\text{b}})}}{\sum \Delta\omega N_{\text{sc}}(\omega_s)}, \tag{24}$$

the two sums being over all spectral channels. The relative error (24) is plotted in figure 7 as a function of v_D/v_{th} for $T_{\text{e}} = 500\text{eV}$ and $Z = 1$; the case of a single laser pulse is reported together with the cases of a burst of 5 and 10 laser pulses. As expected, for low values of v_D/v_{th} the deformations of the distribution function are hardly visible causing the relative error on the current density measurement to blow up. On the other hand, as the drift velocity v_D, and, thus, the electric current density, becomes large, the relative error decreases and drops below 20% at $v_D/v_{\text{th}} \approx 0.03$, when a single pulse is used. For the case of figure 6 ($v_D/v_{\text{th}} = 0.02$), the relative error on the current density amounts to 30% (single pulse), but can be improved considerably by using a longer burst with multiple laser pulses.

7. Analytical estimates and sensitivity of the error to the shape of the electron distribution function. Strictly speaking, the electron distribution function of Spitzer and Härm describes a current density driven by an external electric field (Ohmic current). On the other hand, current densities that are generated by different mechanisms exist in plasmas, such as the bootstrap

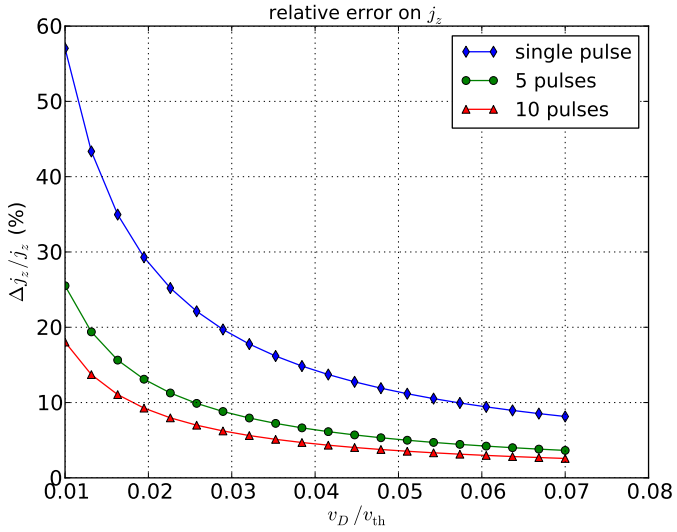

Figure 7: Relative error on the simulated measure of the plasma electric current density as a function of $v_D/v_{\rm th}$, according to equation (24) with signals produced by the Spitzer-Härm distribution function, for the reference scenario $T_{\rm e} = 500$eV, and $Z = 1$. The case of a single laser pulse (blue curve, $\mathcal{E}_i = 20$J) is reported together with the cases of a burst of 5 (green curve, $\mathcal{E}_i = 100$J) and 10 (red curve, $\mathcal{E}_i = 200$J) laser pulses.

current [12]. In addition, as mentioned in the introduction, the distribution function of Spitzer and Härm is obtained under a number of simplifying assumptions that are not strictly fulfilled in a tokamak plasma. It is therefore natural to ask how much sensitive the estimates presented in the last section are to the details of the electron distribution function.

In order to quantify this point, we can compare the expected relative error on the current density measurements corresponding to different electron distribution functions that carry the same current density.

With this aim, let us consider the family of distributions given by

$$f(\vec{v}) = \frac{1}{(\pi v_{\rm th}^2)^{3/2}} e^{-v^2/v_{\rm th}^2} \Big[1 + c_p \frac{\vec{v}_D \cdot \vec{v}}{v_{\rm th}^2} p\big(v/v_{\rm th}\big) \Big], \qquad v_D \ll v_{\rm th}, \tag{25}$$

which is parametrized by a velocity $\vec{v}_D$ and an arbitrary (polynomially bounded) function $p(x) \geq 0$; the normalization constant c_p depends on the choice of the function p, namely,

$$c_p^{-1} = \frac{1}{\sqrt{\pi}} \int_{-\infty}^{+\infty} x^2 e^{-x^2} \Big(\int_0^{+\infty} e^{-w} p(\sqrt{x^2 + w}) dw \Big) dx. \tag{26}$$

This normalization ensures that the vector $\vec{v}_D$ is the electron drift velocity, $\int \vec{v} f(\vec{v}) d^3v = \vec{v}_D$; in addition, by a symmetry argument, it is straightforward to verify that $f(\vec{v})$ is normalized to unity, $\int f(\vec{v}) d^3v = 1$, as it should be.

Equation (25) describes a set of deformations of a Maxwellian distribution function in the direction of the drift velocity $\vec{v}_D$, the deformation being con-

trolled by the ratio $v_D/v_{\rm th} \ll 1$, where $v_{\rm th}$ is the thermal speed. The arbitrary function $p(x)$ controls the shape of the deformation. One can see that $p(x)$ and $\kappa p(x)$ generate the same distribution for any constant $\kappa > 0$.

More precisely, the distribution functions (25) are meant to be approximations only: e.g., for large velocities, these distributions can even become negative. For instance, a special case of the family (25) is the shifted Maxwellian distribution, obtained for

$$p(x) = \text{constant}.$$

(As mentioned above, the exact value of the constant is unessential.) Indeed, for $p = $ constant, equation (25) becomes

$$f(\vec{v}) = \frac{1}{(\pi v_{\rm th}^2)^{3/2}} e^{-v^2/v_{\rm th}^2} \Big[1 + 2\vec{v}_D \cdot \vec{v}/v_{\rm th}^2\Big] \approx \frac{1}{(\pi v_{\rm th}^2)^{3/2}} e^{-\frac{(\vec{v}-\vec{v}_D)^2}{v_{\rm th}^2}}, \qquad (27)$$

which is the first-order expansion of a shifted Maxwellian distribution in the limit $v_D \ll v_{\rm th}$.

The Spitzer-Härm distribution function considered before is included in the family (25) provided that we can find a function $p(x)$ satisfying

$$c_p x p(x) = q g(x),$$

where $g(x)$ is the function given in the paper by Spitzer and Härm, [7]. That amounts to an integral equation for $p(x)$, a solution of which is readily found on noting that the consistency of the Spitzer-Härm distribution requires

$$\vec{v}_D = \int \vec{v} f_{\rm SH}(\vec{v}) d^3v,$$

at least approximately. The integral at the right-hand side is further simplified by choosing a reference frame with $\vec{v}_D$ directed along the third axis; then, the x- and y-components of the integral vanish as they should, and, from the z-component together with $v_{D,z} = v_D$, one has the identity

$$1 = \frac{q}{\sqrt{\pi}} \int_{-\infty}^{+\infty} x^2 e^{-x^2} \Big(\int_0^{+\infty} e^{-w} \frac{g\big(\sqrt{x^2+w}\big)}{\sqrt{x^2+w}} dw \Big) dx.$$

Since $g(x) \sim x^\alpha$ with $\alpha > 1$ for $x \to 0$, the inner integral is well defined, and this shows that $p(x) = qg(x)/x$ gives $c_p = 1$ and is the required function to reproduce the Spitzer-Härm distribution from (25).

The shifted Maxwellian and the Spitzer-Härm distribution are just two examples of deformation of a Maxwellian equilibrium described by (25). It is worth noting that, as far as the parameter $\vec{v}_D$ is kept constant, all elements of the family (25) carry the same current density. Different choices of the function $p(x)$ correspond to different shapes of the deformation, that can be more pronounced on the bulk than on the tails of the distribution function depending on the choice of p.

Let us first compute the generic scattering signal corresponding to an electron distribution function of the form (25). This requires the reduced distribu-

tion (8), which, in this case, reads,

$$h(v_k) = \frac{1}{\sqrt{\pi}v_{\rm th}} e^{-v_k^2/v_{\rm th}^2} + c_p \frac{v_D/v_{\rm th}}{(\pi v_{\rm th}^2)^{3/2}} \int_{-\infty}^{+\infty} dv_x \int_{-\infty}^{+\infty} dv_y e^{-v^2/v_{\rm th}^2} \frac{v}{v_{\rm th}} p(v/v_{\rm th}) \cos\alpha_v.$$

The velocity pitch-angle cosine is dealt with as in section 4, and the second term becomes

$$\frac{v_D v_k}{v_{\rm th}^2} \cos\gamma \frac{1}{(\pi v_{\rm th}^2)^{3/2}} \int_{-\infty}^{+\infty} dv_x \int_{-\infty}^{+\infty} dv_y e^{-v^2/v_{\rm th}^2} p(v/v_{\rm th}),$$

which can be be simplified using cylindrical coordinates with the result that

$$h(v_k) = \frac{1}{\sqrt{\pi}v_{\rm th}} e^{-v_k^2/v_{\rm th}^2} \Big[1 + c_p \Big(\frac{v_D}{v_{\rm th}} \cos\gamma\Big) \frac{v_k}{v_{\rm th}} \hat{p}(v_k/v_{\rm th})\Big], \tag{28}$$

where we have introduced the even function,

$$\hat{p}(x) = \int_0^{+\infty} e^{-w} p(\sqrt{x^2 + w}) dw. \tag{29}$$

With $\tilde{h}(v_k/v_{\rm th}) = v_{\rm th} h(v_k)$, the scattering signal (10) amounts to,

$$N_{{\rm sc},\omega}(\omega_s) = n_{\rm e} H \frac{1}{k v_{\rm th}} \tilde{h}\Big(\frac{\Delta\omega}{k v_{\rm th}}\Big), \tag{30}$$

H being defined in section 3, and

$$\tilde{h}(x) = \frac{1}{\sqrt{\pi}} e^{-x^2} \Big[1 + c_p x_D x \hat{p}(x)\Big], \qquad x_D = (v_D/v_{\rm th}) \cos\gamma. \tag{31}$$

Multiplication by the width $\Delta\omega_s$ of spectral channels gives the number of collected photoelectrons in each channel, namely,

$$N_{\rm sc}(\omega_s) = n_{\rm e} H \frac{\Delta\omega_s}{k v_{\rm th}} \tilde{h}\Big(\frac{\Delta\omega}{k v_{\rm th}}\Big). \tag{32}$$

Since $\hat{p}$ is even, the second term in $\tilde{h}$ is odd and we can readily compute the total number of scattering photoelectrons,

$$N_{\rm sc,tot} = n_{\rm e} H \frac{1}{k v_{\rm th}} \int \tilde{h}\Big(\frac{\Delta\omega}{k v_{\rm th}}\Big) d\omega_s = n_{\rm e} H \int \tilde{h}(x) dx = n_{\rm e} H,$$

which is related to the electron density, cf. equation (11).

The signal (32) is directly proportional to the function $\tilde{h}$, which, on the other hand, depends on the particular choice of the shape function p. Figure 8 shows the scattering signal $N_{\rm sc} - N_{\rm sc,Max}$ normalized to $N_{\rm sc,tot}\Delta\omega_s/(k v_{\rm th})$ according to equation (32), for three choices of the function $p(x)$ and for $x_D = 0.02$; $N_{\rm sc,Max}$ is the signal corresponding to the Maxwellian distribution. One can see how the shape of the deformation can be modeled by changing the function $p(x)$. Specifically, the blue curve corresponds to the shifted Maxwellian distribution realized by setting $p(x) = 1$: in this case, the maximum of the deformation is attained

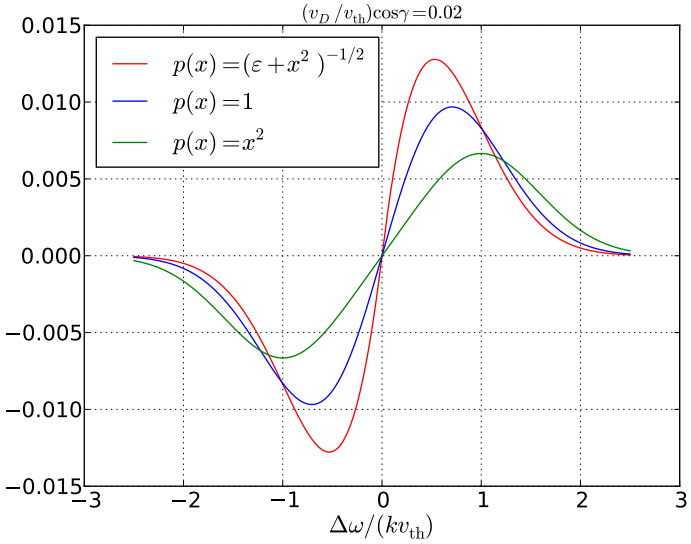

Figure 8: Normalized difference between the signal $N_{\rm sc}$, equation (32), and the corresponding Maxwellian equilibrium for three different choices of the function $p(x)$ and for $x_D = 0.02$, $\varepsilon = 10^{-3}$. The intermediate case (blue curve) corresponds to a shifted Maxwellian distribution.

well within the thermal bulk of the equilibrium distribution, $\Delta\omega \leq \Delta\omega_{\rm th} = kv_{\rm th}$. The green curve corresponds to $p(x) = x^2$, which has an asymptotic behavior for $x \to 0$ similar to that of the Spitzer-Härm distribution: in this case, the maximum of the deformation is attained at about one thermal speed; higher powers $p(x) = x^n$, $n > 2$, would shift the deformation further on the tails of the equilibrium distribution. At last, the red curve corresponds to a mathematical model, which is shown just as an example without implying any specific physical meaning, namely, $p(x) = (\varepsilon + x^2)^{-1/2}$, with $\varepsilon = 10^{-3}$: this choice shifts the deformation very much on the bulk of the distribution.

The current density carried by the electrons is, equation (13),

$$j_z = \frac{e}{H} n_{\rm e} H \frac{1}{kv_{\rm th}} \int \frac{\Delta\omega}{k} \tilde{h}\Big(\frac{\Delta\omega}{kv_{\rm th}}\Big) d\omega_s = e n_{\rm e} v_{\rm th} \int x\tilde{h}(x) dx.$$

The remaining integral can be computed using the normalization condition (26),

$$\int x\tilde{h}(x)dx = x_D \frac{c_p}{\sqrt{\pi}} \int x^2 e^{-x^2} \hat{p}(x) dx = x_D = (v_D/v_{\rm th}) \cos\gamma,$$

hence,

$$j_z = e n_{\rm e} v_D \cos\gamma, \tag{33}$$

as expected: the electric current density does not depend on the particular choice of the shape function p; all the elements of the family of distributions (25) carry the same current density.

An estimate of the relative error associated to the current density j_z can also be computed analytically. One regards the integral (13) as an infinite sum

of Poissonian variables, hence, the variance of the current density is the integral of the variance of the integrand in (13) plus the background. That is,

$$\sigma^2 = \frac{e^2}{H^2} \int \Big(\frac{\Delta\omega}{k}\Big)^2 \big(N_{\mathrm{sc},\omega} + 2N_{\mathrm{b},\omega}\big) d\omega_s. \tag{34}$$

The integral involving the scattering signal amounts to

$$\int \Big(\frac{\Delta\omega}{k}\Big)^2 N_{\mathrm{sc},\omega} d\omega_s = n_{\mathrm{e}} H v_{\mathrm{th}}^2 \int x^2 \tilde{h}(x) dx,$$

and, recalling that $\hat{p}(x)$ is even,

$$\int x^2 \tilde{h}(x) dx = \frac{1}{2} + c_p x_D \frac{1}{\sqrt{\pi}} \int x^3 \hat{p}(x) e^{-x^2} dx = \frac{1}{2}.$$

As for the background light, we use the model put forward in section 5, which relates the background level to the total number of scattering photoelectrons,

$$N_{\mathrm{b},\omega} = \mu_{\mathrm{b}} \frac{N_{\mathrm{sc,tot}}}{2\Delta\omega_{\mathrm{th}}} = \mu_{\mathrm{b}} \frac{n_{\mathrm{e}} H}{2\Delta\omega_{\mathrm{th}}}.$$

Despite this is not consistent with the above treatment of the scattering signal, for which the whole spectrum is taken into account, let us integrate the background signal over a spectral band of half-length $\xi\Delta\omega_{\mathrm{th}}$,

$$\int \Big(\frac{\Delta\omega}{k}\Big)^2 N_{\mathrm{b},\omega} d\omega_s = \mu_{\mathrm{b}} \frac{n_{\mathrm{e}} H v_{\mathrm{th}}^2}{2\Delta\omega_{\mathrm{th}}} k v_{\mathrm{th}} \int_{-\xi}^{+\xi} x^2 dx = \frac{1}{3} \xi^3 \mu_{\mathrm{b}} n_{\mathrm{e}} H v_{\mathrm{th}}^2,$$

where the definition $\Delta\omega_{\mathrm{th}} = k v_{\mathrm{th}}$ has been used. The combination of the foregoing results gives the variance

$$\sigma^2 = \frac{e^2 n_{\mathrm{e}} v_{\mathrm{th}}^2}{H} \Big[\frac{1}{2} + \frac{2}{3}\xi^3 \mu_{\mathrm{b}}\Big],$$

which, in particular, is independent of the choice of the function p, provided that ξ is chosen independently of p; we shall see, however, that it can be convenient to adapt the band-width ξ to the shape p of the deformation.

We can now write an analytical estimate of the relative error for the measurement of the electric current density when the electron distribution is approximated by one of the elements of the family (25); that reads,

$$\frac{\Delta j_z}{j_z} = \frac{v_{\mathrm{th}}}{v_D \cos\gamma} \Big[\frac{1 + 4\xi^3 \mu_{\mathrm{b}}/3}{2N_{\mathrm{sc,tot}}}\Big]^{1/2}. \tag{35}$$

Again, this is independent of the particular choice of the element of the family (25), unless the band-width ξ is adapted to the shape of the deformation. One can also note that, $\Delta j_z/j_z$ is inversely proportional to the strength v_D/v_{th} of the deformation, as well as to $\cos\gamma$.

The foregoing analytical result, although appealing, should be applied with some care. Firstly, in order to get nice analytical expressions, we have taken into account the scattering signal over the whole spectrum, while, in reality, the diagnostics is sensitive to a limited spectral band only. Moreover, using a

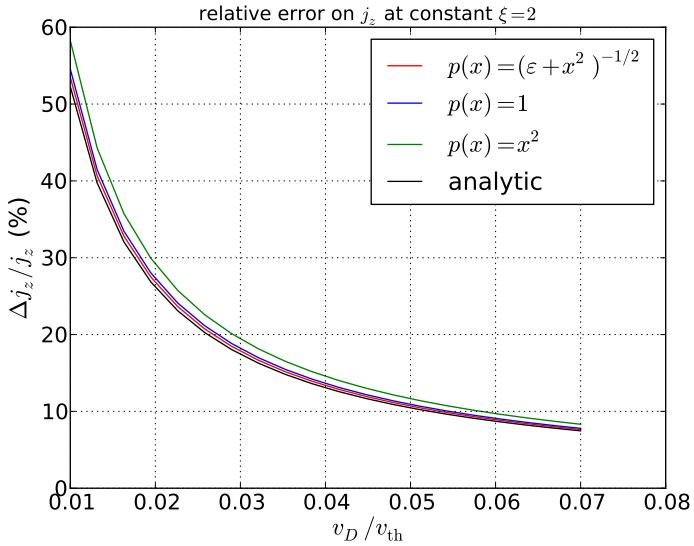

Figure 9: Relative error of the simulated current density measurement according to equation (24), for the three cases of figure 8. The analytical estimate (35) is also shown (black curve). Here, the band width ξ of the diagnostics is the same for all cases.

continuous integration, rather than a discrete sum over channels does not allow us to estimate the discretization error.

In figure 9, the relative error for the current density is displayed for the three cases of figure 8, holding the band width constant at the value $\xi = 2$, for all the three cases. The error is computed using the discretized form (24), with the parameters of the reference ASDEX Upgrade setup discussed in section 6, and for a single laser pulse. The corresponding discretization errors are 3.26% for the bulk-shifted deformation model (red curve), 5.14% for the shifted Maxwellian model (blue curve), and 11.18% for the quadratic deformation model (green curve). The analytical estimate, equation (35), is also shown for reference (black curve). One can see that, with the band width ξ being kept constant, the relative error depends only weakly on the shape function $p(x)$, as expected from the analytical estimate. The weak dependence, which is not described by the analytical theory, appears to be related to the discretization error: the smaller that is, the closer the result is to the analytical prediction. Indeed, the current density obtained from the simulated measurement, equation (23), underestimates the exact value, thus leading to a larger relative error with respect to the analytical estimate.

So far the band width observed by the diagnostics has been held constant, with the result that the relative error does not vary significantly with the shape of the distribution function, while the discretization error does depend on it. Conversely, one can adapt the band width ξ to the electron distribution function in order to keep the theoretical discretization error constant. In this case, the analytical estimate (35) suggests a dependence of the relative error on the shape of the distribution: ξ, and, thus, the error, is smaller for those functions p that

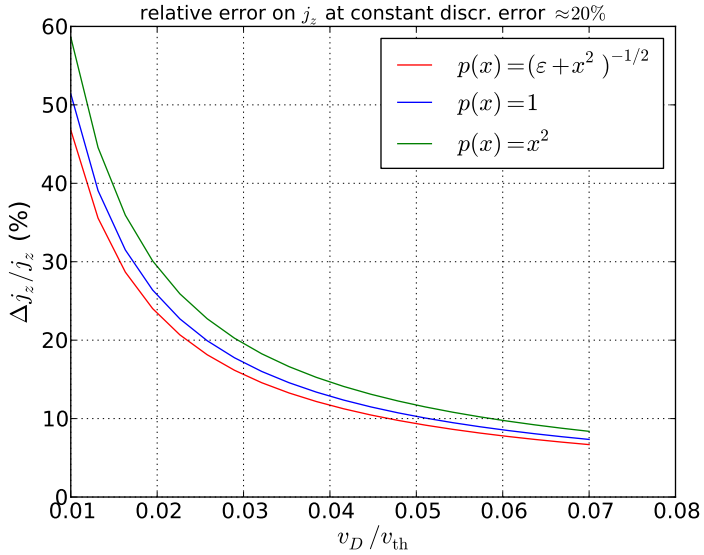

Figure 10: The same as in figure 9, but with the band width ξ adapted so that, for each curve, the theoretical discretization error is $\approx 20\%$.

are shifted on the bulk.

Figure 10 shows the results of the simulated current density measurement, when the band width ξ of the diagnostics is adapted to the shape of the distribution so that the theoretical discretization error is about 20% for all the three considered cases. The obtained values of the spectral band-width are $\xi = 1.35$ (red curve), $\xi = 1.49$ (blue curve), and $\xi = 1.77$ (green curve); that corresponds to 59, 65, and 77 spectral channels, respectively. Those results have been obtained by means of an iterative process that reduces the band width ξ by an amount $\Delta\xi$ corresponding to the width of a spectral channel, starting from a large initial guess; the iteration is stopped as soon as the discretization error becomes equal or larger than a given threshold (20% is the case of figure 10). The final discretization error is not exactly equal to the threshold value: for the three cases of figure 10 that is 20.7%, 21.36%, and 20.45%, respectively. As a consequence of the variable band width, a difference between the three cases is now clearly visible, but still relatively small. The error is smaller for the bulk-shifted distributions (red and blue curves), that allow us to use a narrower spectral window, and, thus, to collect less background light. It is worth noting, however, that, in this case, the relative error due to the statistical fluctuations and background light is comparable to the discretization error for $v_D/v_{\mathrm{th}} \geq 0.02$.

The analysis of figures 9 and 10 appears to indicate that, for a given value of the electric current density j_z carried by the electrons, the order of magnitude of the relative error on j_z is not sensitive to the shape of the electron distribution function, although it can be advantageous to adapt the spectral band-width of the diagnostics to the shape of the expected theoretical electron distribution, cf. figure 10.

8. Conclusions. The foregoing analysis provides a rough framework for the evaluation of the feasibility of the Thomson scattering measurement of the fraction of the plasma electric current density carried by the electrons.

The signal coming from a Spitzer-Härm electron distribution function has been evaluated for the parameters of the proposed experimental setup [1, 2] and the results have been used for the feasibility study reported by Tsalas et al. [2].

Particularly, figure (6) shows that, for the reference case, the noise is larger than the difference of signals with and without current density. This emphasizes how difficult the measurement of the current density can be.

The whole electric current density measurement has been simulated and the expected error has been estimated and plotted in figure 7. For a single laser pulse, with $T_\mathrm{e} = 500\mathrm{eV}$, $Z = 1$, and for values of v_D/v_th larger than 0.03, the relative error on the electric current density drops below 20%. The error can be further reduced by making use of laser bursts with multiple pulses, at the price of reducing the temporal resolution.

Let us recall the limitations of these calculations. The Spitzer-Härm distribution function does not account for the effects of the confining magnetic field, i.e. magnetic trapping effects are neglected. The inclusion of the effect of the inhomogeneous magnetic field requires the numerical solution of the kinetic equation. Relativistic effects should also be properly addressed by considering the relativistic equivalent of the Spitzer-Härm distribution function obtained by Braams and Karney [13]. Moreover, the error estimate (24) does not account for the propagation of errors through the various devices in the experimental setup, such as photomultipliers, that may alter the Poisson distribution of the number of photoelectrons per channel. At last, the Spitzer-Härm distribution is not justified for the description of non-Ohmic current densities.

In view of all the these limitations, it is natural to question the robustness of the error estimate obtained from the Spitzer-Härm distribution. The analysis presented in section 7 addresses precisely this issue on the basis of a family of model distribution functions, which is general enough to include both the Spitzer-Härm and the shifted Maxwellian distributions. This analysis suggests that, the order of magnitude of the relative error can be considered independent of the details of the distribution function. An improvement of the accuracy of the measurement is, however, possible if the width of the spectral window observed by the diagnostics is adapted to the expected theoretical model for the electron distribution function. This makes a precise theoretical modeling of the electrons even more important for an optimal analysis of Thomson scattering data.

Acknowledgments. We wish to thank Mikhail Kantor, Maximos Tsalas, Elisabeth Wolfrum and Bernd Kurzan for the enlightening discussions on the experimental setup, and for stimulating our interest in this study.

References

[1] M. Kantor, Conceptual design of Thomson scattering diagnostics on ASDEX-UPGRADE (2010).

[2] M. Tsalas, M. Kantor, O. Maj, R. Bilato, P. C. de Vries, A. J. H. Donnè, A. Herrmann, B. Kurzan and E. Wolfrum, Journal of Instrumentation **7**, C03015 (2011).

[3] J. Sheffield, Plasma Physics 14 (1972) 783.

[4] S. E. Segre, in Course on Plasma Diagnostics and Data Acquisition Systems, Varenna International School of Plasma Physics, p. 265, Bologna, 1975, Editrice Composition.

[5] S. E. Segre, Plasma Physics 20 (1978) 287.

[6] U. Carretta, A. Jacchia, G. Lampis, et al., Il Nuovo Cimento B (1971-1996) 55 (1980) 229, 10.1007/BF02739156.

[7] L. Spitzer and R. Härm, Phys. Rev. 89 (1953) 977.

[8] I. H. Hutchinson, Journal of Physics D: Applied Physics 10 (1977) L11.

[9] F. Alladio and M. Martone, Physics Letters A 64 (1977) 199.

[10] J. Lasalle and P. Platz, Plasma Phys. 20 (1978) 107.

[11] M. Kantor, Private Communication 2010.

[12] A. G. Peeters, Plasma Phys. Control. Fusion **42**, B231B242 (2000).

[13] B. J. Braams and C. F. F. Karney, Phys. Fluids B 1 (1989) 1355.